DRAFT VERSION JANUARY 14, 2013
Preprint typeset using LaTeX style emulateapj v. 08/22/09

arXiv:1301.2595v1 [astro-ph.SR] 11 Jan 2013

EFFECTS OF STRONG STRATIFICATION ON EQUATORWARD DYNAMO WAVE PROPAGATION

PETRI J. KÄPYLÄ[1,2], MAARIT J. MANTERE[1,3], ELIZABETH COLE[1], JÖRN WARNECKE[2,4] AND AXEL BRANDENBURG[2,4]
[1]Physics Department, Gustaf Hällströmin katu 2a, PO Box 64, FI-00014 University of Helsinki, Finland
[2]NORDITA, KTH Royal Institute of Technology and Stockholm University, Roslagstullsbacken 23, SE-10691 Stockholm, Sweden
[3]Aalto University, Department of Information and Computer Science, PO Box 15400, FI-00076 Aalto, Finland
[4]Department of Astronomy, AlbaNova University Center, Stockholm University, SE-10691 Stockholm, Sweden
Draft version January 14, 2013

ABSTRACT

We present results from simulations of rotating magnetized turbulent convection in spherical wedge geometry representing parts of the latitudinal and longitudinal extents of a star. Here we consider a set of runs for which the density stratification is varied, keeping the Reynolds and Coriolis numbers at similar values. In the case of weak stratification we find quasi-steady solutions for moderate rotation and oscillatory dynamos with poleward migration of activity belts for more rapid rotation. For stronger stratification a similar transition as a function of the Coriolis number is found, but with an equatorward migrating branch near the equator. We test the domain size dependence of our results for a rapidly rotating run with equatorward migration by varying the longitudinal extent of our wedge. The energy of the axisymmetric mean magnetic field decreases as the domain size increases and we find that an $m = 1$ mode is excited for a full 2π ϕ-extent, reminiscent of the field configurations deduced from observations of rapidly rotating late-type stars.

Subject headings: Magnetohydrodynamics – convection – turbulence – Sun: dynamo, rotation, activity

1. INTRODUCTION

The large-scale magnetic field of the Sun, manifested by the 11 year sunspot cycle, is generally believed to be generated within or just below the turbulent convection zone (e.g. Ossendrijver 2003, and references therein). The latter concept is based on the idea that the strong shear in the tachocline just beneath the convection zone amplifies the toroidal magnetic field which then becomes buoyantly unstable and erupts to the surface (e.g. Parker 1955b). This process has been adopted in many mean-field models of the solar cycle in the form of a non-local α-effect (e.g. Kitchatinov & Olemskoy 2012) in conjunction with a reduced turbulent diffusivity within the convection zone, and a single cell anti-clockwise meridional circulation which acts as a conveyor belt for the magnetic field. These so-called flux transport models (e.g. Dikpati & Charbonneau 1999) are now widely used to study the solar cycle and even to predict its future course (Dikpati & Gilman 2006; Choudhuri et al. 2007).

The flux transport paradigm is, however, facing several theoretical challenges: 10^5 gauss magnetic fields are expected to reside in the tachocline (D'Silva & Choudhuri 1993), but such fields are difficult to explain with dynamo theory (Guerrero & Käpylä 2011) and may have become unstable at much lower field strengths (Arlt et al. 2005). Furthermore, the low value of turbulent diffusion within the convection zone seems unlikely (e.g. Käpylä et al. 2009). In addition, the meridional circulation pattern of the Sun can be more complicated than that required in the flux-transport models (Hathaway 2011; Miesch et al. 2012). These difficulties have led to a revival of the distributed dynamo (e.g. Brandenburg 2005; Pipin 2012) in which magnetic fields are generated throughout the convection zone due to turbulent effects (e.g. Krause & Rädler 1980; Käpylä et al. 2006; Pipin & Seehafer 2009).

Early studies of self-consistent three-dimensional magnetohydrodynamic (MHD) simulations of convection in spherical coordinates produced oscillatory large-scale dynamos (Gilman 1983; Glatzmaier 1985), but the dynamo wave was found to propagate towards the poles rather than the equator as in the Sun. More recent anelastic large-eddy simulations (LES) with rotation rates somewhat higher than that of the Sun have produced non-oscillatory (Brown et al. 2010) and oscillatory (Brown et al. 2011; Nelson et al. 2013) large-scale magnetic fields, depending essentially on the rotation rate and the vigor of the turbulence. However, similar models with the solar rotation rate have either failed to produce an appreciable large-scale component (Brun et al. 2004) or, more recently, oscillatory solutions with almost no latitudinal propagation of the activity belts (Ghizaru et al. 2010; Racine et al. 2011). These simulations covered a full spherical shell and used realistic values for solar luminosity and rotation rate, necessitating the use of anelastic solvers and spherical harmonics (e.g. Brun et al. 2004) or implicit methods (e.g. Ghizaru et al. 2010). Here we exploit an alternative approach by modeling fully compressible convection in wedge geometry (see also Robinson & Chan 2001) with a finite-difference method. We omit the polar regions and cover usually only a part of the longitudinal extent, e.g. $90°$ instead of the full $360°$. At the cost of omitting connecting flows across the poles and introducing artificial boundaries there, the gain is that higher spatial resolution can be achieved. Furthermore, retaining the sound waves can be beneficial when considering possible helio- or asteroseismic applications. Recent hydrodynamic (Käpylä et al. 2011a,b) and MHD (Käpylä et al. 2010) studies with this method have shown that this approach produces results that are in accordance with fully spherical models. Moreover, the first turbulent dynamo solution with solar-like migration properties of the magnetic field was recently obtained using this type of setup (Käpylä et al. 2012b). Extended setups that include a coronal layer as a more realistic upper radial boundary have been successful in producing dynamo-driven coronal ejections (Warnecke et al. 2012). As we show in a companion paper (Warnecke et al. 2013), a solar-like differential rotation pattern might be another conse-

Electronic address: petri.kapyla@helsinki.fi (Revision: 1.153)

quence of including an outer coronal layer.

Here we concentrate on exploring further the recent discovery of equatorward migration in spherical wedge simulations (Käpylä et al. 2012b). In particular, we examine a set of runs for which the rotational influence on the fluid, measured by the Coriolis number, which is also called the inverse Rossby number, is kept approximately constant while the density stratification of the simulations is gradually increased.

2. THE MODEL

Our model is the same as that in Käpylä et al. (2012a). We model a wedge in spherical polar coordinates, where (r,θ,ϕ) denote radius, colatitude, and longitude. The radial, latitudinal, and longitudinal extents of the wedge are $r_0 \le r \le R$, $\theta_0 \le \theta \le \pi-\theta_0$, and $0 \le \phi \le \phi_0$, respectively, where R is the radius of the star and $r_0 = 0.7\,R$ denotes the position of the bottom of the convection zone. Here we take $\theta_0 = \pi/12$ and in most of our models we use $\phi_0 = \pi/2$, so we cover a quarter of the azimuthal extent between $\pm 75^\circ$ latitude. We solve the compressible hydromagnetics equations[1],

$$\frac{\partial \boldsymbol{A}}{\partial t} = \boldsymbol{u}\times\boldsymbol{B} - \eta\mu_0\boldsymbol{J}, \tag{1}$$

$$\frac{D\ln\rho}{Dt} = -\boldsymbol{\nabla}\cdot\boldsymbol{u}, \tag{2}$$

$$\frac{D\boldsymbol{u}}{Dt} = \boldsymbol{g} - 2\boldsymbol{\Omega}_0\times\boldsymbol{u} + \frac{1}{\rho}\left(\boldsymbol{J}\times\boldsymbol{B} - \boldsymbol{\nabla}p + \boldsymbol{\nabla}\cdot 2\nu\rho\mathsf{S}\right), \tag{3}$$

$$T\frac{Ds}{Dt} = \frac{1}{\rho}\left[\boldsymbol{\nabla}\cdot\left(\boldsymbol{F}^{\rm rad}+\boldsymbol{F}^{\rm SGS}\right) + \mu_0\eta\boldsymbol{J}^2\right] + 2\nu\mathsf{S}^2, \tag{4}$$

where $\boldsymbol{A}$ is the magnetic vector potential, $\boldsymbol{u}$ is the velocity, $\boldsymbol{B}=\boldsymbol{\nabla}\times\boldsymbol{A}$ is the magnetic field, $\boldsymbol{J}=\mu_0^{-1}\boldsymbol{\nabla}\times\boldsymbol{B}$ is the current density, η is the magnetic diffusivity, μ_0 is the vacuum permeability, $D/Dt=\partial/\partial t+\boldsymbol{u}\cdot\boldsymbol{\nabla}$ is the advective time derivative, ν is the kinematic viscosity, ρ is the density,

$$\boldsymbol{F}^{\rm rad} = K\boldsymbol{\nabla}T \quad\text{and}\quad \boldsymbol{F}^{\rm SGS} = \chi_{\rm SGS}\rho T\boldsymbol{\nabla}s \tag{5}$$

are the radiative and subgrid scale (SGS) heat fluxes, where K is the radiative heat conductivity and $\chi_{\rm SGS}$ turbulent heat conductivity, which represents the unresolved convective transport of heat and was referred to as $\chi_{\rm t}$ in Käpylä et al. (2012a), s is the specific entropy, T is the temperature, and p is the pressure. The fluid obeys the ideal gas law with $p=(\gamma-1)\rho e$, where $\gamma = c_{\rm P}/c_{\rm V} = 5/3$ is the ratio of specific heats at constant pressure and volume, respectively, and $e=c_{\rm V}T$ is the internal energy.

The gravitational acceleration is given by $\boldsymbol{g}=-GM\hat{\boldsymbol{r}}/r^2$, where G is the gravitational constant, M is the mass of the star, and $\hat{\boldsymbol{r}}$ is the unit vector in the radial direction. In simulations, the maximum possible Rayleigh number is much smaller than in real stars, which implies a larger Mach number. The rotation vector $\boldsymbol{\Omega}_0$ is given by $\boldsymbol{\Omega}_0 = \Omega_0(\cos\theta,-\sin\theta,0)$. However, to have realistic Coriolis numbers, the angular velocity in the Coriolis force is increased correspondingly, but that in the centrifugal force is omitted, as it would otherwise be unrealistically large (cf. Käpylä et al. 2011b). The rate of strain tensor S is given by

$$\mathsf{S}_{ij} = \tfrac{1}{2}(u_{i;j}+u_{j;i}) - \tfrac{1}{3}\delta_{ij}\boldsymbol{\nabla}\cdot\boldsymbol{u}, \tag{6}$$

where the semicolons denote covariant differentiation (Mitra et al. 2009).

2.1. *Initial and boundary conditions*

The initial state is isentropic and the hydrostatic temperature gradient is given by

$$\frac{\partial T}{\partial r} = -\frac{GM/r^2}{c_{\rm V}(\gamma-1)(n+1)}, \tag{7}$$

where $n=1.5$ is the polytropic index. We fix the value of $\partial T/\partial r$ on the lower boundary. The density profile follows from hydrostatic equilibrium. The heat conduction profile is chosen so that radiative diffusion is responsible for supplying the energy flux in the system, with K decreasing more than two orders of magnitude from bottom to top (Käpylä et al. 2011a). A weak random small-scale seed magnetic field is taken as initial condition (see below).

The radial and latitudinal boundaries are assumed to be impenetrable and stress free, i.e.,

$$u_r = 0, \quad \frac{\partial u_\theta}{\partial r} = \frac{u_\theta}{r}, \quad \frac{\partial u_\phi}{\partial r} = \frac{u_\phi}{r} \quad (r=r_0,R), \tag{8}$$

$$\frac{\partial u_r}{\partial\theta} = u_\theta = 0, \quad \frac{\partial u_\phi}{\partial\theta} = u_\phi\cot\theta \quad (\theta=\theta_0,\pi-\theta_0). \tag{9}$$

For the magnetic field we assume perfect conductors at the lower radial and latitudinal boundaries, and radial field at the outer radial boundary. In terms of the magnetic vector potential these translate to

$$\frac{\partial A_r}{\partial r} = A_\theta = A_\phi = 0 \quad (r=r_0), \tag{10}$$

$$A_r = 0, \ \frac{\partial A_\theta}{\partial r} = -\frac{A_\theta}{r}, \ \frac{\partial A_\phi}{\partial r} = -\frac{A_\phi}{r} \quad (r=R), \tag{11}$$

$$A_r = \frac{\partial A_\theta}{\partial\theta} = A_\phi = 0 \quad (\theta=\theta_0,\pi-\theta_0). \tag{12}$$

We use small-scale low amplitude Gaussian noise as initial condition for the magnetic field. On the latitudinal boundaries we assume that the thermodynamic quantities have vanishing first derivatives, thus suppressing heat fluxes through the boundaries.

On the upper boundary we apply a black body condition

$$\sigma T^4 = -K\frac{\partial T}{\partial r} - \chi_{\rm SGS}\rho T\frac{\partial s}{\partial r}, \tag{13}$$

where σ is the Stefan–Boltzmann constant. We use a modified value for σ that takes into account that our Reynolds and Rayleigh numbers are much smaller than in reality, so K and therefore the energy flux through the domain are much larger than in the Sun.

2.2. *Dimensionless parameters*

To facilitate with other work using different normalizations, we present our results in this paper by normalizing with physically meaningful quantities. We note, however, that in the code we used non-dimensional quantities by choosing

$$R = GM = \rho_0 = c_{\rm P} = \mu_0 = 1, \tag{14}$$

where ρ_0 is the initial density at $r=r_0$. The units of length, time, velocity, density, entropy, and magnetic field are therefore

$$[x]=R, \ \ [t]=\sqrt{R^3/GM}, \ \ [u]=\sqrt{GM/R}, \\ \rho=\rho_0, \ \ [s]=c_{\rm P}, \ \ [B]=\sqrt{\rho_0\mu_0 GM/R}. \tag{15}$$

[1] Note that in Equation (4) of Käpylä et al. (2012b) the Ohmic heating term $\mu_0\eta\boldsymbol{J}^2$ and a factor ρ in the viscous dissipation term $2\nu\mathsf{S}^2$ were omitted, but they were actually included in the calculations.

Our simulations are defined by the energy flux imposed at the bottom boundary, $F_{\rm b} = -(K\partial T/\partial r)|_{r=r_0}$, the temperature at the top boundary, $T_1 = T(r = R)$, as well as the values of Ω_0, ν, η, and $\overline{\chi}_{\rm SGS} = \chi_{\rm SGS}(r_{\rm m} = 0.85\,R)$. Furthermore, the radial profiles of K and $\chi_{\rm SGS}$ need to be specified. The corresponding nondimensional input parameters are the luminosity parameter

$$\mathcal{L} = \frac{L_0}{\rho_0 (GM)^{3/2} R^{1/2}}, \tag{16}$$

the normalized pressure scale height at the surface,

$$\xi = \frac{(\gamma-1) c_{\rm V} T_1}{GM/R}, \tag{17}$$

the Taylor number

$$\mathrm{Ta} = (2\Omega_0 R^2/\nu)^2, \tag{18}$$

the fluid and magnetic Prandtl numbers

$$\mathrm{Pr} = \frac{\nu}{\overline{\chi}_{\rm SGS}}, \quad \mathrm{Pm} = \frac{\nu}{\eta}, \tag{19}$$

and the non-dimensional viscosity

$$\tilde{\nu} = \frac{\nu}{\sqrt{GMR}}. \tag{20}$$

Instead of ξ, we often quote the resulting density contrast, $\Gamma_\rho \equiv \rho(r_0)/\rho(R)$.

Other useful diagnostic parameters are the fluid and magnetic Reynolds numbers

$$\mathrm{Re} = \frac{u_{\rm rms}}{\nu k_{\rm f}}, \quad \mathrm{Rm} = \frac{u_{\rm rms}}{\eta k_{\rm f}}, \tag{21}$$

and the Coriolis number

$$\mathrm{Co} = \frac{2\Omega_0}{u_{\rm rms} k_{\rm f}}, \tag{22}$$

where $u_{\rm rms} = \sqrt{(3/2)\langle u_r^2 + u_\theta^2\rangle_{r\theta\phi t}}$ is the rms velocity and the subscripts indicate averaging over θ, ϕ, and a time interval during which the turbulence is statistically stationary. Note that for $u_{\rm rms}$ we omit the contribution from the azimuthal velocity, because its value is dominated by effects from the differential rotation (Käpylä et al. 2011b). The Taylor number can also be written as $\mathrm{Ta} = \mathrm{Co}^2\mathrm{Re}^2(k_{\rm f}R)^4$, with $k_{\rm f}R \approx 21$. Due to the fact that the initial stratification is isentropic, we quote the turbulent Rayleigh number $\mathrm{Ra_t}$ from the thermally relaxed state of the run,

$$\mathrm{Ra_t} = \frac{GM(\Delta r)^4}{\nu \overline{\chi}_{\rm SGS} R^2} \left(-\frac{1}{c_{\rm P}} \frac{\mathrm{d}\langle s\rangle_{\theta\phi t}}{\mathrm{d}r} \right)_{r_{\rm m}}, \tag{23}$$

where $k_{\rm f} = 2\pi/\Delta r$ is an estimate of the wavenumber of the largest eddies, and $\Delta r = R - r_0 = 0.3R$ is the thickness of the layer. We also quote the value of $k_\omega = \omega_{\rm rms}/u_{\rm rms}$, where $\boldsymbol{\omega} = \boldsymbol{\nabla} \times \boldsymbol{u}$ and $\omega_{\rm rms}$, is the volume averaged rms value of $\boldsymbol{\omega}$. The magnetic field is expressed in equipartition field strengths, $B_{\rm eq}(r) = \langle \mu_0 \rho \boldsymbol{u}^2 \rangle^{1/2}_{\theta\phi t}$, where all three components of $\boldsymbol{u}$ are included. We define mean quantities as averages over the ϕ-coordinate and denote them by overbars. However, as we will see, there can also be significant power in low-order spherical harmonic modes with azimuthal order $m = 1$ and 2, which will be discussed at the end of the paper.

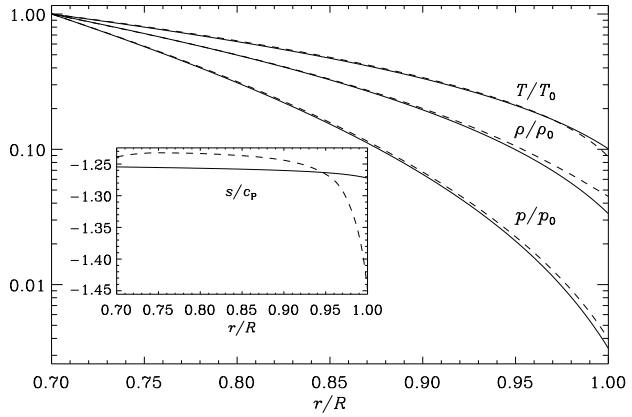

FIG. 1.— Initial (solid lines) and saturated (dashed) radial profiles of temperature T, density ρ, and pressure p, normalized by their respective values at the bottom of the domain from Run C1 (indicated by subscript zero). The inset shows the specific entropy $s/c_{\rm P}$ from the same run.

The simulations were performed with the PENCIL CODE[2], which uses a high-order finite difference method for solving the compressible equations of magnetohydrodynamics.

3. RESULTS

We perform runs for four values of ξ, corresponding to initial density stratifications $\Gamma_\rho = 2, 5, 30$, and 100. These runs are referred to as series A–D. In series E we use $\Gamma = 30$ and vary ϕ_0 with all other parameters being kept the same as in Run C1. For each series we consider different values of Co and Re. The hydrodynamic progenitors of the Runs B1, C1, and D1 correspond to Runs A4, B4, and C4 from Käpylä et al. (2011a). The rest of the simulations were run from the initial conditions described in Section 2.1.

Earlier studies applying fully spherical simulations have shown that organized large-scale magnetic fields appear provided the rotation of the star is rapid enough (Brown et al. 2010) and that at even higher rotation rates, cyclic solutions with poleward migration are obtained (Brown et al. 2011). A similar transition has been observed in spherical wedge models of Käpylä et al. (2010) and Käpylä et al. (2012a). However, in the former case the oscillatory mode showed poleward migration of the activity belts whereas in the latter an equatorward branch appears near the equator. Furthermore, in the runs of Käpylä et al. (2012a) the dynamo mode changes from one showing a high frequency cycle with poleward migration near the equator to another mode with lower frequency and equatorward migration when the magnetic field becomes dynamically important.

There are several differences between the models of Käpylä et al. (2010) and Käpylä et al. (2012a): the amount of density stratification (a density contrast of 3 in comparison to 30), efficiency of convective energy transport (20 per cent versus close to 100 per cent in the majority of the domain), and the top boundary condition for entropy (constant temperature versus black body radiation). Here we concentrate on studying the influence of the density stratification on models similar to those presented in Käpylä et al. (2012a).

3.1. *Thermal boundary effects and energy balance*

In Käpylä et al. (2011a) we started to apply the black body boundary condition, Equation (13), that has previously been used in mean-field models with thermodynamics

[2] http://code.google.com/p/pencil-code/

TABLE 1
SUMMARY OF THE RUNS.

Run	grid	Pr	Pm	Ta	ξ	Γ_ρ	$\tilde{\nu}$	$\mathcal{L}$	$\mathrm{Ra_t}$	Re	Rm	Co
A1	$128\times256\times128$	1.5	1.0	10^{10}	0.29	2	$1.7\cdot10^{-5}$	$3.8\cdot10^{-5}$	$8.3\cdot10^{5}$	26	26	8.6
A2	$128\times256\times128$	1.5	1.0	$1.8\cdot10^{10}$	0.29	2	$1.7\cdot10^{-5}$	$3.8\cdot10^{-5}$	$1.1\cdot10^{5}$	24	24	12.8
B1	$128\times256\times128$	2.5	1.0	$6.4\cdot10^{9}$	0.09	5	$2.9\cdot10^{-5}$	$3.8\cdot10^{-5}$	$1.1\cdot10^{6}$	22	22	8.1
B2	$128\times256\times128$	2.5	1.0	$1.4\cdot10^{10}$	0.09	5	$2.9\cdot10^{-5}$	$3.8\cdot10^{-5}$	$1.1\cdot10^{6}$	20	20	13.7
C1	$128\times256\times128$	2.5	1.0	$1.4\cdot10^{10}$	0.02	30	$2.9\cdot10^{-5}$	$3.8\cdot10^{-5}$	$2.1\cdot10^{6}$	35	35	7.8
C2	$128\times256\times128$	2.5	1.0	$4.0\cdot10^{10}$	0.02	30	$2.9\cdot10^{-5}$	$3.8\cdot10^{-5}$	$2.7\cdot10^{6}$	31	31	14.8
D1	$128\times256\times128$	7.5	3.0	$1.6\cdot10^{9}$	0.008	100	$4.7\cdot10^{-5}$	$6.3\cdot10^{-6}$	$1.2\cdot10^{6}$	11	34	8.0
D2	$256\times512\times256$	4.0	2.0	10^{10}	0.008	100	$2.5\cdot10^{-5}$	$6.3\cdot10^{-6}$	$2.4\cdot10^{6}$	25	50	9.1
E1	$128\times256\times64$	2.5	1.0	$1.4\cdot10^{10}$	0.02	30	$2.9\cdot10^{-5}$	$3.8\cdot10^{-5}$	$2.1\cdot10^{6}$	34	34	7.9
E2	$128\times256\times128$	2.5	1.0	$1.4\cdot10^{10}$	0.02	30	$2.9\cdot10^{-5}$	$3.8\cdot10^{-5}$	$2.1\cdot10^{6}$	35	35	7.8
E3	$128\times256\times256$	2.5	1.0	$1.4\cdot10^{10}$	0.02	30	$2.9\cdot10^{-5}$	$3.8\cdot10^{-5}$	$2.4\cdot10^{6}$	35	35	7.9
E4	$128\times256\times256$	2.5	1.0	$1.4\cdot10^{10}$	0.02	30	$3.5\cdot10^{-5}$	$3.8\cdot10^{-5}$	$2.2\cdot10^{6}$	28	28	8.1

NOTE. — The second to ninth columns show quantities which are input parameters to the models whereas the quantities in the last four columns are results of the simulations computed from the saturated state. Here we use $\phi_0=\pi/2$ in Sets A–D. In Set E we use $\phi_0=\pi/4$ (Run E1), $\phi_0=\pi/2$ (E2), $\phi_0=\pi$ (E3), and $\phi_0=2\pi$ (E4). Runs C1 and E2 are the same model, and is also the same as Run B4m of Käpylä et al. (2012a).

TABLE 2
SUMMARY OF DIAGNOSTIC VARIABLES.

Run	$\tilde{\lambda}$	$E_{\rm mer}/E_{\rm kin}$	$E_{\rm rot}/E_{\rm kin}$	$E_{\rm mag}/E_{\rm kin}$	$E_{\rm pol}/E_{\rm mag}$	$E_{\rm tor}/E_{\rm mag}$	$\Delta_\Omega^{(r)}$	$\Delta_\Omega^{(\theta)}$	k_ω
A1	0.084	0.000	0.580	0.418	0.045	0.396	0.013	0.089	62
A2	0.095	0.000	0.490	0.553	0.068	0.338	0.009	0.050	62
B1	0.028	0.000	0.705	0.345	0.038	0.487	0.034	0.142	68
B2	0.098	0.000	0.757	0.222	0.056	0.427	0.023	0.072	72
C1	0.006	0.001	0.440	0.346	0.138	0.203	0.047	0.068	93
C2	0.105	0.001	0.326	0.706	0.198	0.238	0.016	0.030	94
D1	0.003	0.002	0.222	0.472	0.166	0.135	0.011	-0.000	89
D2	0.003	0.000	0.617	0.222	0.133	0.190	0.045	0.058	116
E1	0.007	0.001	0.478	0.393	0.133	0.328	0.048	0.069	92
E2	0.006	0.001	0.440	0.346	0.138	0.203	0.047	0.068	93
E3	0.005	0.001	0.375	0.380	0.120	0.172	0.037	0.055	92
E4	0.024	0.001	0.363	0.470	0.065	0.114	0.035	0.050	91

NOTE. — Here $\tilde{\lambda}=\lambda/(u_{\rm rms}k_{\rm f})$ is the normalized growth rate of the magnetic field. $E_{\rm kin}=\frac{1}{2}\langle\rho\boldsymbol{u}^2\rangle$ is the volume averaged kinetic energy. $E_{\rm mer}=\frac{1}{2}\langle\rho(\overline{u}_r^2+\overline{u}_\theta^2)\rangle$ and $E_{\rm rot}=\frac{1}{2}\langle\rho\overline{u}_\theta^2\rangle$ denote the volume averaged energies of the azimuthally averaged meridional circulation and differential rotation. Analogously $E_{\rm mag}=\frac{1}{2}\langle\boldsymbol{B}^2\rangle$ is the total volume averaged magnetic energy while $E_{\rm pol}=\frac{1}{2}\langle(\overline{B}_r^2+\overline{B}_\theta^2)\rangle$ and $E_{\rm tor}=\frac{1}{2}\langle\overline{B}_\theta^2\rangle$ are the energies in the axisymmetric part of the poloidal and toroidal magnetic fields.

(Brandenburg et al. 1992). Instead of using the physical value for the Stefan–Boltzmann constant, we estimate the value of σ so that the flux at the upper boundary is approximately that needed to transport the total luminosity of the star through the surface. However, the final thermally relaxed state of the simulation can significantly deviate from the initial state. In combination with the nonlinearity of Equation (13), the final stratification is usually somewhat different from the initial one; see Figure 1 for an illustrative example from Run C1. The final density stratification in this case is around 22, down from 30 in the initial state.

The main advantage of the black body condition is that it allows the temperature at the surface more freedom than in our previous models where a constant temperature is imposed (Käpylä et al. 2010, 2011b). Furthermore, as the temperature is allowed to vary at the surface, this can be used as a diagnostic for possible irradiance variations. These are discussed further in Section 3.6.

Considering the energy balance, we show the energy fluxes for Run E4 in Figure 2. We find that the simulation is thermally relaxed and that the total luminosity is close to the input luminosity, i.e. $L_{\rm tot}-L_0\sim0$. The fluxes are defined as:

$$\overline{F}_{\rm rad}=-K\frac{\partial\langle T\rangle}{\partial r}, \tag{24}$$

$$\overline{F}_{\rm conv}=c_{\rm P}\langle(\rho u_r)'T'\rangle, \tag{25}$$

$$\overline{F}_{\rm kin}=-\tfrac{1}{2}\langle(\rho u_r)'\boldsymbol{u}'^2\rangle, \tag{26}$$

$$\overline{F}_{\rm visc}=-2\nu\langle(\rho u_i)'S_{ir}\rangle, \tag{27}$$

$$\overline{F}_{\rm turb}=-\chi_{\rm SGS}\langle\rho\rangle\langle T\rangle\frac{\partial\langle s\rangle}{\partial r}, \tag{28}$$

$$\overline{F}_{\rm Poyn}=\langle E_\theta B_\phi-E_\phi B_\theta\rangle/\mu_0, \tag{29}$$

where $\boldsymbol{E}=\eta\mu_0\boldsymbol{J}-\boldsymbol{u}\times\boldsymbol{B}$, the primes denote fluctuations, and angle brackets averaging over θ, ϕ, and a time interval over which the turbulence is statistically stationary. The radiative flux carries energy into the convection zone and drops steeply as a function of radius so that it contributes only a few per cent in the middle of the convection zone. The resolved convection is responsible for transporting the energy through the majority of the layer, whereas the unresolved turbulent transport carries energy through the outer surface. The other contributions are much smaller. The flux of kinetic energy is also very small in the rapid rotation regime considered here (see also Augustson et al. 2012).

3.2. *Dynamo excitation and large-scale magnetic fields*

The azimuthally averaged toroidal magnetic fields from all runs listed in Table 1 are shown in Figures 3–6. The full time

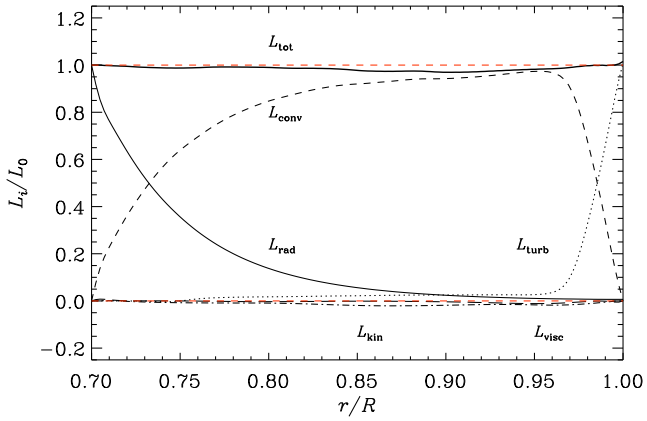

FIG. 2.— Luminosity of the energy fluxes from Run E4: radiative conduction (thin solid line), enthalpy (dashed), kinetic energy (dot-dashed), viscous (long dashed), and unresolved subgrid scale (dotted) fluxes. The thick solid line is the sum of all contributions. The two dashed red lines indicate the zero and unity line.

evolution from the introduction of the seed magnetic field to the final saturated state is shown for each run. Although the magnitude of the seed field in terms of the equipartition strength is different in each set, already a visual inspection suggests that the growth rate of the dynamo is greater in the cases with low stratification. The measured average growth rates over the kinematic stage,

$$\lambda = \langle d \ln B_{\rm rms}/dt \rangle_t, \tag{30}$$

support this conjecture; see the second column of Table 2. Comparing Runs A1, B1, C1, and D2 with roughly comparable Reynolds and Coriolis number shows that the normalized growth rate decreases monotonically from 0.084 in Run A1 to just 0.003 in Run D2. Another striking feature is that λ increases by a factor of nearly 20 from Run C1 to C2 where the only difference between the runs is that the latter has a roughly two times higher Coriolis number. It turns out that in all of the cases (Runs A1, A2, B1, B2, C2, and E4) with the highest growth rates, a poleward migrating dynamo mode at low latitudes is excited first. In some of the runs this mode is later overcome by another one that can be quasi-stationary (Runs A1 and B1) or oscillatory with equatorward migration and a much longer cycle period (Runs C2 and E4).

In Figure 3 we show the azimuthally averaged toroidal magnetic field $\overline{B}_\phi$ near the surface of the computational domain ($r = 0.98\,R$) for two runs (A1 and A2; see Table 1) with $\Gamma_\rho = 2$ (Set A). We find that in Run A1 with ${\rm Co} \approx 8.7$ the mean magnetic field is initially oscillatory with poleward propagation of the activity belts. At $tu_{\rm rms}k_{\rm f} \approx 400$ the dynamo mode changes to a quasi-steady configuration. In Run A2 a poleward mode persists throughout the simulation, although the oscillation period is irregular and significant hemispherical asymmetry exists. This behavior is similar to the runs presented in Käpylä et al. (2010) which are comparable in terms of stratification, Coriolis and Reynolds numbers.

In Set B with $\Gamma_\rho = 5$ the situation is similar: in Run B1 with ${\rm Co} \approx 8.1$ there is a poleward mode with a short cycle period near the equator which is visible from early times, see Figure 4. However, after around $tu_{\rm rms}k_{\rm f} = 1200$ there is a dominating non-oscillatory mode which is especially clear at high latitudes. There are still hints of the poleward mode near the equator. In Run B2 with ${\rm Co} \approx 13.7$, however, the poleward mode prevails also at late times. As in Run A2, the cycles show significant variability and hemispheric asymmetry.

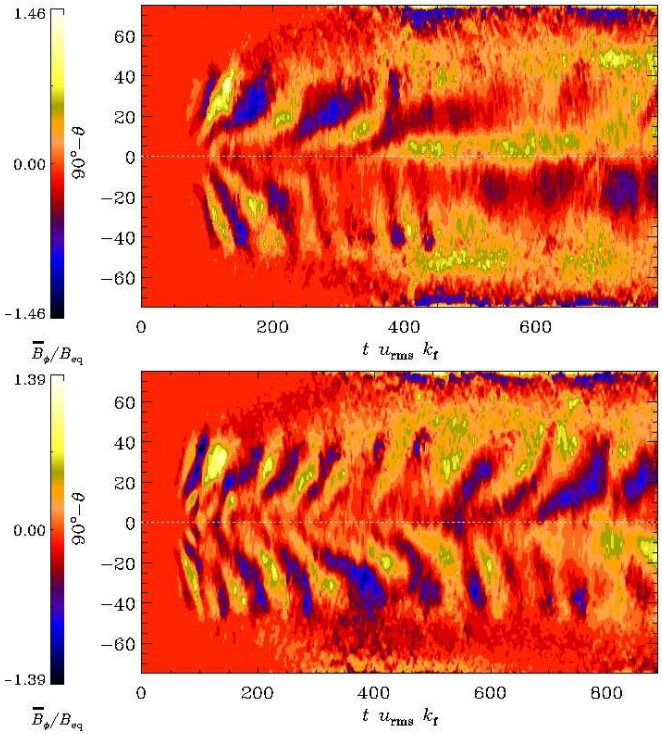

FIG. 3.— $\overline{B}_\phi$ near the surface of the star at $r = 0.98\,R$ as a function of latitude ($= 90° - \theta$) for Runs A1 (top) and A2 (bottom). The white dotted line denotes the equator $90° - \theta = 0$.

The runs in Sets A and B also show signs of non-axisymmetric 'nests' of convection (cf. Busse 2002; Brown et al. 2008) in the hydrodynamical and kinematic stages. Once the magnetic field is strong enough these modes either vanish or they are significantly damped.

Increasing the stratification further to $\Gamma_\rho = 30$ (Set C) the dynamo solutions at lower rotation rates, ${\rm Co} \lesssim 5$, are still quasi-steady; see Figure 2 of Käpylä et al. (2012a). However, a watershed regarding the oscillatory modes at higher Co seems to have been reached so that the irregular poleward migration seen in Sets A and B is replaced by more regular equatorward patterns. In Run C1 with ${\rm Co} \approx 8.7$ the poleward migration near the equator is secondary to the equatorward mode—even in the kinematic stage; see Figure 5. The poleward mode near the equator is more prominent in the early stages of Run C2 with ${\rm Co} \approx 14.7$, but also there it is subdominant at late times.

For $\Gamma_\rho = 100$ (Set D) the general picture is similar to that in Set C. Quasi-steady configurations at lower rotation change into equatorward migrating solutions at sufficiently high Co. We find this transition to occur between ${\rm Co} = 5$ and 8, similarly as in Set C. For Set D the equatorward mode is visible for both runs; see Figure 4. In Run D1 no poleward migration at low latitudes is seen in the kinematic stage. Also the poleward migrating branch at high latitudes is missing in the non-linear stage. Both of these features are present in Run D2.

To connect our results with observations of magnetically active stars we compute the ratio of the dynamo cycle frequency and the rotation rate, $\omega_{\rm cyc}/\Omega_0$. Plotting this ratio as a function of the Coriolis number for stars exhibiting chromospheric activity has shown that stars tend to group along inactive and active branches (Brandenburg et al. 1998), and for higher Coriolis numbers along a super-active branch (Saar & Brandenburg 1999). Six of our simulations

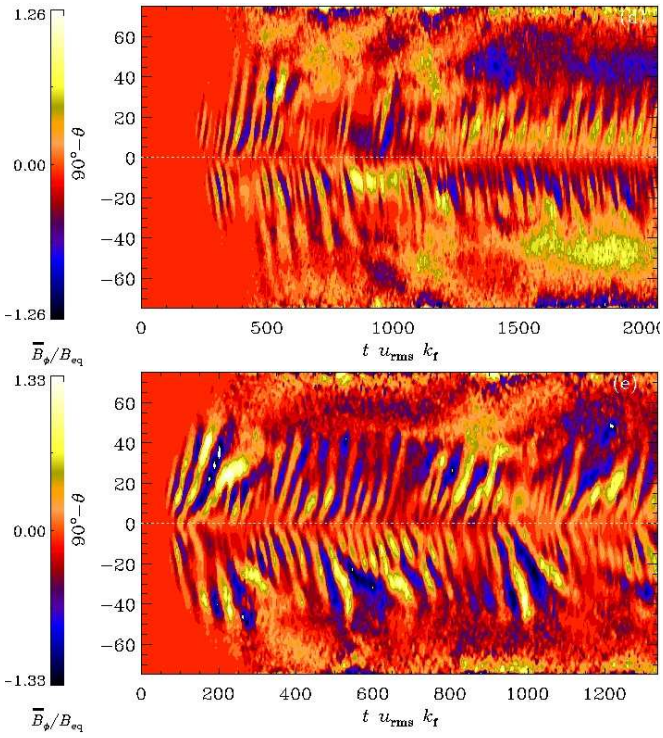

FIG. 4.— Same as Figure 3 but for Runs B1 (top) and B2 (bottom).

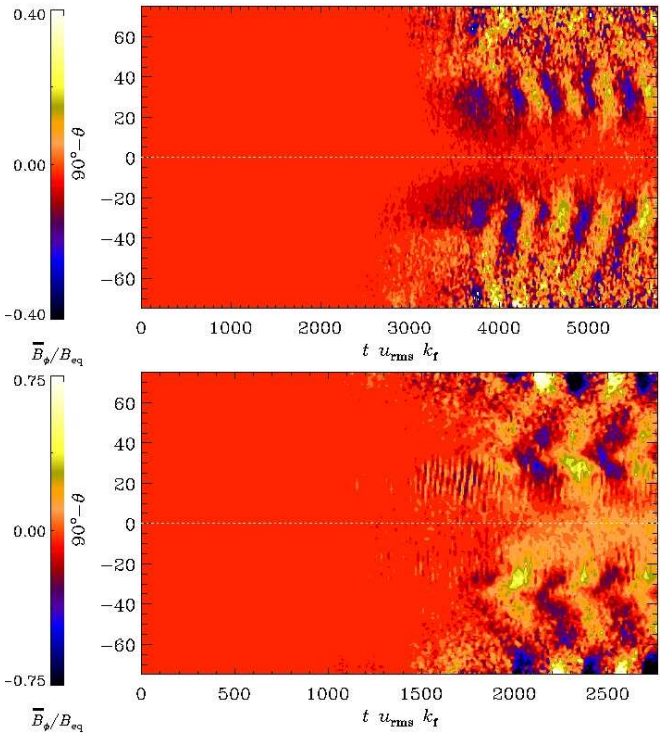

FIG. 6.— Same as Figure 3 but for Runs D1 (top panel) and D2 (bottom).

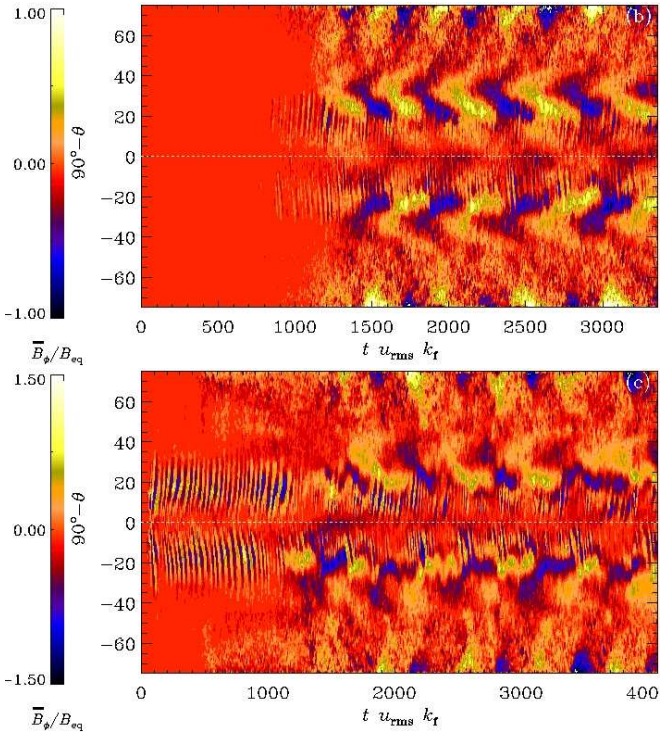

FIG. 5.— Same as Figure 3 but for Runs C1 (top panel) and C2 (bottom). Note the difference in cycle frequency between early times when the frequency is similar to that of Run B2 (Figure 4) and late times.

(Runs A2, B2, C1, C2, D1, and D2), excluding the runs in Set E which are very similar to each other and Run C1 in this respect, show cycles and can be thus used in this analysis. For Runs C1, C2, D1, and D2 the cycle frequency was measured from a few latitudes on both hemispheres and for all available cycles individually. The final result is an average over the individually computed values. In two of our models (Runs A2 and B2) the cycle periods vary irregularly. There the cycle frequency is computed from the highest peak of a temporal Fourier transformation of the time series for $\overline{B}_\phi$ at low latitudes near the surface. The results are shown in the upper panel of Figure 7.

The association with real branches in Figure 7 is clearly premature, because we cannot be sure that there are no stars connecting the group of Runs C1, D1, D2 with that of A2 and B2 through a single line with a larger slope. Nevertheless, this plot allows us to see that, while the separation in the ratio $\omega_{\rm cyc}/\Omega_0$ is slightly less for the two groups of runs, compared with active and inactive stars, their relative ordering in the value of Co is actually the other way around. One would therefore not have referred to Runs A2 and B2 as inactive just because their $\omega_{\rm cyc}/\Omega_0$ ratio agrees with that of inactive stars. In fact, their $E_{\rm mag}/E_{\rm kin}$ ratios in Table 2 are typically larger than for Runs C1, D1, D2.

As is clear from the inset of the upper panel of Figure 7, there is no clear relation between Co and $E_{\rm mag}/E_{\rm kin}$, which is clearly different from stars for which there is a clear relation between Co (referred to as inverse Rossby number in that context) and stellar activity (a measure of $E_{\rm mag}/E_{\rm kin}$); see Brandenburg et al. (1998) for details and references. Furthermore, there is also no clear indication of two branches in the graph of $\omega_{\rm cyc}/\Omega_0$ versus $E_{\rm mag}/E_{\rm kin}$; see the lower panel of Figure 7. Instead, there might just be one group in it, possibly with a positive correlation, i.e., $\omega_{\rm cyc}/\Omega_0$ might increase with $E_{\rm mag}/E_{\rm kin}$. As discussed by Brandenburg et al. (1998), a positive slope would not be easy to explain in the framework of standard mean-field dynamo theory, where the frequency ratio is usually a decreasing function of normalized rotation rate and activity parameter.

In conclusion, we can say that the quantity $\omega_{\rm cyc}/\Omega_0$ is an

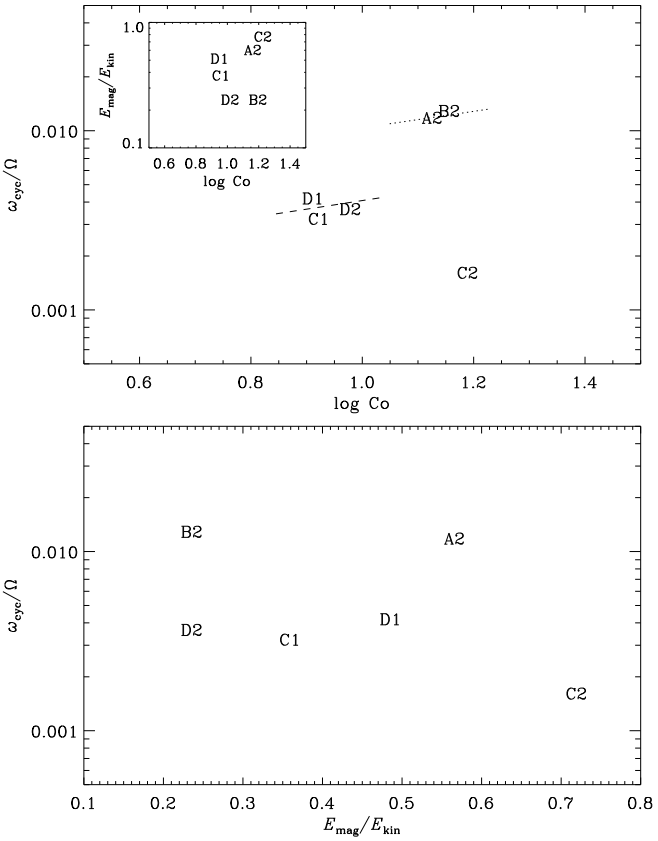

FIG. 7.— Ratio of the dynamo cycle and rotation frequencies from six runs which show cyclic activity as functions of rotation (upper panel) and the ratio of magnetic to kinetic energy (lower panel). The dotted and dashed lines in the upper are given by $c_i \mathrm{Co}^{\sigma_i}$, where the σ_i correspond to those in Brandenburg et al. (1998), and c_i are used as fit parameters. The inset in the top panel show the ratio $E_{\rm mag}/E_{\rm kin}$ as a function of Co.

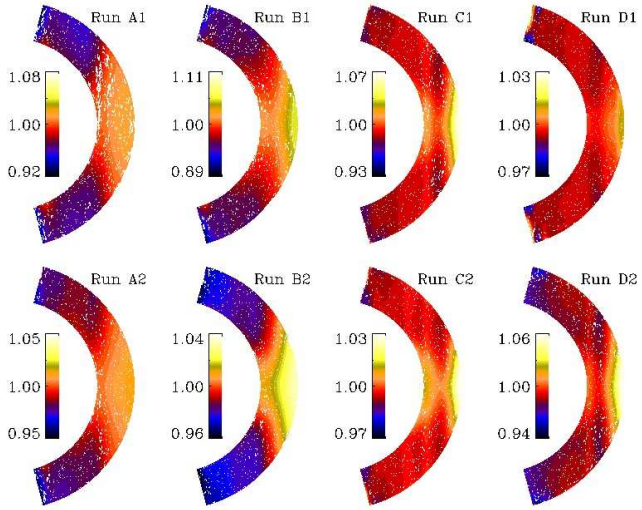

FIG. 8.— Mean rotation profile $\overline{\Omega}/\Omega_0$ (contours) and meridional circulation $\boldsymbol{u}_{\rm m} = (\overline{u}_r, \overline{u}_\theta, 0)$ (arrows) from Sets A, B, C, and D.

important and robust property of any cyclic dynamo model and its dependence on other properties of the model should therefore be a useful characteristics that can be compared with other models and ultimately with actual stars. Here we have just make a first attempt in classifying model results in this sense.

3.3. *Differential rotation and meridional circulation*

Non-uniform rotation of the convection zone of the Sun is an important ingredient in maintaining the large-scale magnetic field. Furthermore, the sign of the radial gradient of the mean angular velocity plays a crucial role in deciding whether the dynamo wave propagates towards the pole or the equator in mean-field models (e.g. Parker 1955a, 1987). In the following we use the local angular velocity defined as $\overline{\Omega} = \overline{u_\phi}/r\sin\theta + \Omega_0$. Azimuthally averaged rotation profiles from the runs in Sets A to D are shown in Figure 8. The rotation profiles of Runs E1, E3, and E4 are very similar to that of Run C1. We quantify the radial and latitudinal differential rotation by

$$\Delta_\Omega^{(r)} = \frac{\overline{\Omega}_{\rm eq} - \overline{\Omega}_{\rm bot}}{\overline{\Omega}_{\rm eq}}, \tag{31}$$

$$\Delta_\Omega^{(\theta)} = \frac{\overline{\Omega}_{\rm eq} - \overline{\Omega}_{\rm pole}}{\overline{\Omega}_{\rm eq}}, \tag{32}$$

where $\overline{\Omega}_{\rm eq} = \overline{\Omega}(R, \pi/2)$ and $\overline{\Omega}_{\rm bot} = \overline{\Omega}(r_0, \pi/2)$ are the angular velocities at the top and bottom at the equator, respectively, and $\overline{\Omega}_{\rm pole} = \frac{1}{2}[\overline{\Omega}(R,\theta_0) + \overline{\Omega}(R, \pi - \theta_0)]$.

Mean-field and LES models of stellar rotation are most often performed without including magnetic fields (e.g. Rempel 2005; Kitchatinov & Rüdiger 2005; Miesch et al. 2006). This can be misleading because magnetic fields affect the turbulence giving rise to Reynolds stress and a heat flux (e.g. Kitchatinov et al. 1994; Käpylä et al. 2004). Furthermore, the large-scale flows are directly influenced by the Lorentz force when the magnetic field is strong enough (e.g. Malkus & Proctor 1975). A decrease of $\Delta_\Omega^{(\theta)}$ has also been observed in LES models (e.g. Brun et al. 2004). Comparing the latitudinal differential rotation in Run B1 with that of otherwise identical hydrodynamic Run A4 of Käpylä et al. (2011a), we find that $\Delta_\Omega^{(\theta)}$ decreases only slightly from 0.15 to 0.14. For $\Delta_\Omega^{(r)}$ the change is more dramatic from 0.079 to 0.034. The fraction of kinetic energy contained in the differential rotation drops from 0.91 to 0.71. A similar decrease is observed in Run C1 in comparison to its hydrodynamical parent Run B4 of Käpylä et al. (2011a) with $\Delta_\Omega^{(\theta)}$ changing from 0.08 to 0,07, $\Delta_\Omega^{(r)}$ from 0.066 to 0.047, and $E_{\rm rot}/E_{\rm kin}$ dropping from 0.58 to 0.44.

We see a rapidly spinning equator with a positive radial gradient of $\overline{\Omega}$ in all cases; see Figure 8. The latitudinal variation of angular velocity is however not always monotonic and there can be local minima at mid-latitudes, as is seen for example in Run C1. Similar features have been seen before (see, e.g., Miesch et al. 2000; Käpylä et al. 2011b) and might be related to the lack of small-scale turbulence. Especially at larger stratification one would expect smaller-scale turbulent structures to emerge, but this requires sufficient resolution and thus large enough Reynolds numbers, which is not currently possible.

The amount of latitudinal differential rotation is clearly less than in the Sun where $\Delta_\Omega^{(\theta)} \approx 0.2$ between the equator and latitude 60° (e.g. Schou et al. 1998). Furthermore, $\Delta_\Omega^{(\theta)}$ generally decreases within each set of runs as Co increases with the exception of Runs D1 and D2. However, in Run D1 the lower Reynolds number possibly contributes to the weak differential rotation in comparison to Run D2

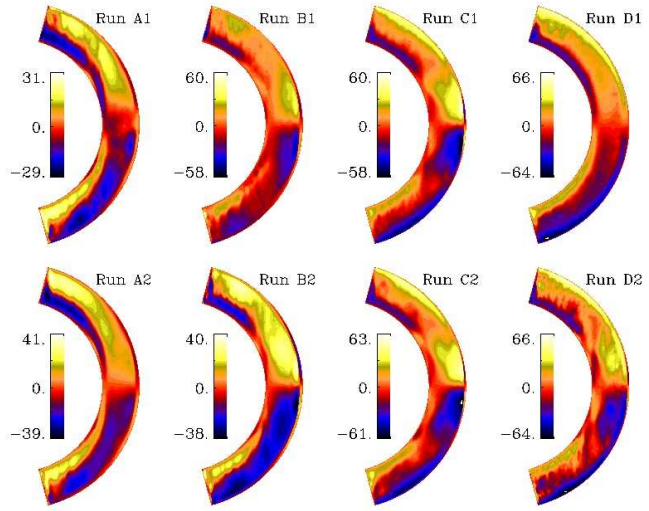

FIG. 9.— Dynamo number C_α from Sets A, B, C, and D.

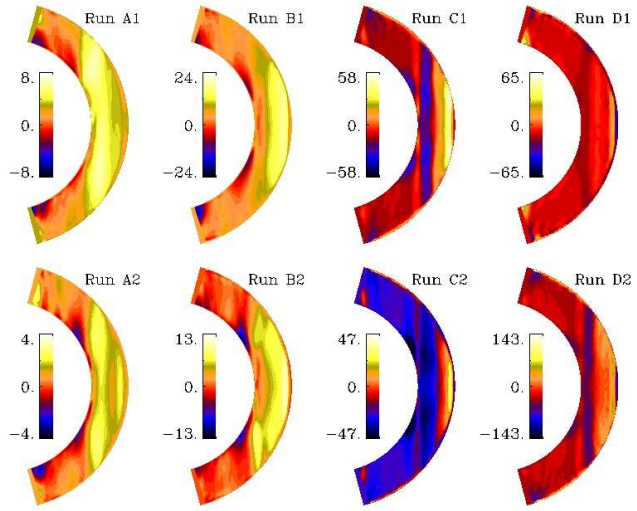

FIG. 10.— Dynamo number C_Ω from Sets A, B, C, and D. We omit regions closer to 2.5° from the latitudinal boundaries.

with comparable Co. The rotation profiles appear to be dominated by the Taylor-Proudman balance except at very low latitudes where the baroclinic term is significant. In a companion paper (Warnecke et al. 2013), we show that an outer coronal layer seems to favor a solar-like rotation, which shows even radially outward pointing contours of constant rotation. Such 'spoke-like' rotation profiles have so far been obtained only in mean-field models involving anisotropic heat transport (e.g. Brandenburg et al. 1992) or a subadiabatic tachocline (Rempel 2005), and in LES models where a latitudinal entropy gradient is enforced at the lower boundary (Miesch et al. 2006).

The meridional circulation is weak in all cases and typically shows multiple cells in radius. The circulations are mostly concentrated in the equatorial regions outside the inner tangent cylinder. This is similar to earlier results by Käpylä et al. (2012a) where the meridional circulation pattern was shown in larger magnification. In addition, as we will show below, the strength of meridional circulation relative to the turbulent magnetic diffusivity is rather low, which is another reason why it cannot play an important role in our models.

3.4. *Estimates of dynamo numbers*

We estimate the dynamo numbers related to the α-effect, radial differential rotation, and the meridional circulation by

$$C_\alpha = \frac{\alpha \Delta R}{\eta_{\rm t0}}, \quad C_\Omega = \frac{\partial \overline{\Omega}/\partial r (\Delta R)^3}{\eta_{\rm t0}}, \quad C_U = \frac{\overline{u}_{\rm mer}^{\rm rms} \Delta R}{\eta_{\rm t0}}, \tag{33}$$

where $\partial\overline{\Omega}/\partial r$ is the r- and θ-dependent radial gradient of $\overline{\Omega}$ and α is a proxy of the α-effect

$$\alpha = -\tfrac{1}{3}\tau(\overline{\boldsymbol{\omega}\cdot\boldsymbol{u}} - \overline{\boldsymbol{j}\cdot\boldsymbol{b}}/\overline{\rho}), \tag{34}$$

with $\tau = \alpha_{\rm MLT} H_{\rm P}/u_{\rm rms}(r,\theta)$ being the convective turnover time and $\alpha_{\rm MLT}$ the mixing length parameter. We use $\alpha_{\rm MLT} = 5/3$ in this work. We estimate the turbulent diffusivity by $\eta_{\rm t0} = \frac{1}{3} u_{\rm rms}(r,\theta)\alpha_{\rm MLT} H_{\rm P}$. Furthermore, $\overline{u}_{\rm mer}^{\rm rms} = \sqrt{\overline{u}_r^2 + \overline{u}_\theta^2}$ is the rms value of the meridional circulation.

The results for the dynamo numbers are shown in Figures 9–11. Generally, the values of C_α are fairly large, and those of C_Ω surprisingly small, suggesting that the dynamos might mainly be of α^2 type. In the following, however, we focus on relative changes between different runs. It turns out that there is a weak tendency for C_α to increase as a function of Γ_ρ and Co. In Set B, however, C_α decreases by a third from Run B1 to B2. The spatial distribution of C_α becomes more concentrated near the boundaries as Γ_ρ increases.

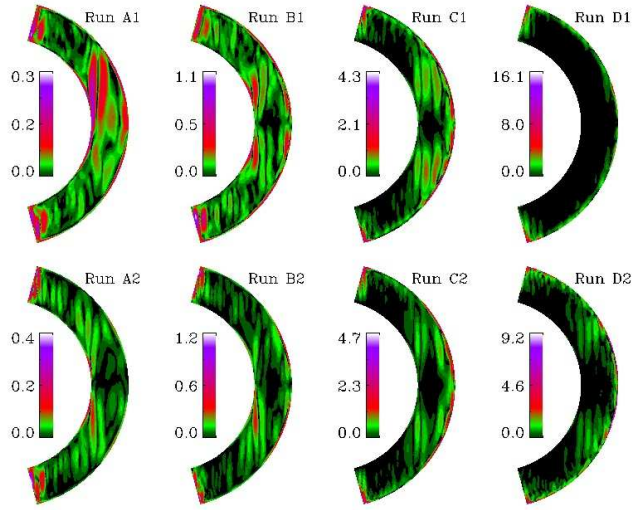

FIG. 11.— Dynamo number C_U from Sets A, B, C, and D.

We find that the effect of the differential rotation is strongest near the equator in all cases. In Sets A and B the absolute values of C_Ω are clearly smaller that those of C_α. This is surprising given the fact that the energy of the toroidal mean field is greater than that of the poloidal field by a significant factor which would be expected if differential rotation dominates over the α-effect in maintaining the field. In Runs C1, C2, and D1 C_α and C_Ω have comparable magnitudes whereas in Run D2 the maximum of C_α is roughly twice that of C_Ω. However, in these cases the toroidal and poloidal field energies are roughly comparable.

We find that C_U is always small in comparison to both C_α and C_Ω. Figure 11 also shows the concentration of coherent meridional circulation cells in the equatorial regions with a multi-cell structure.

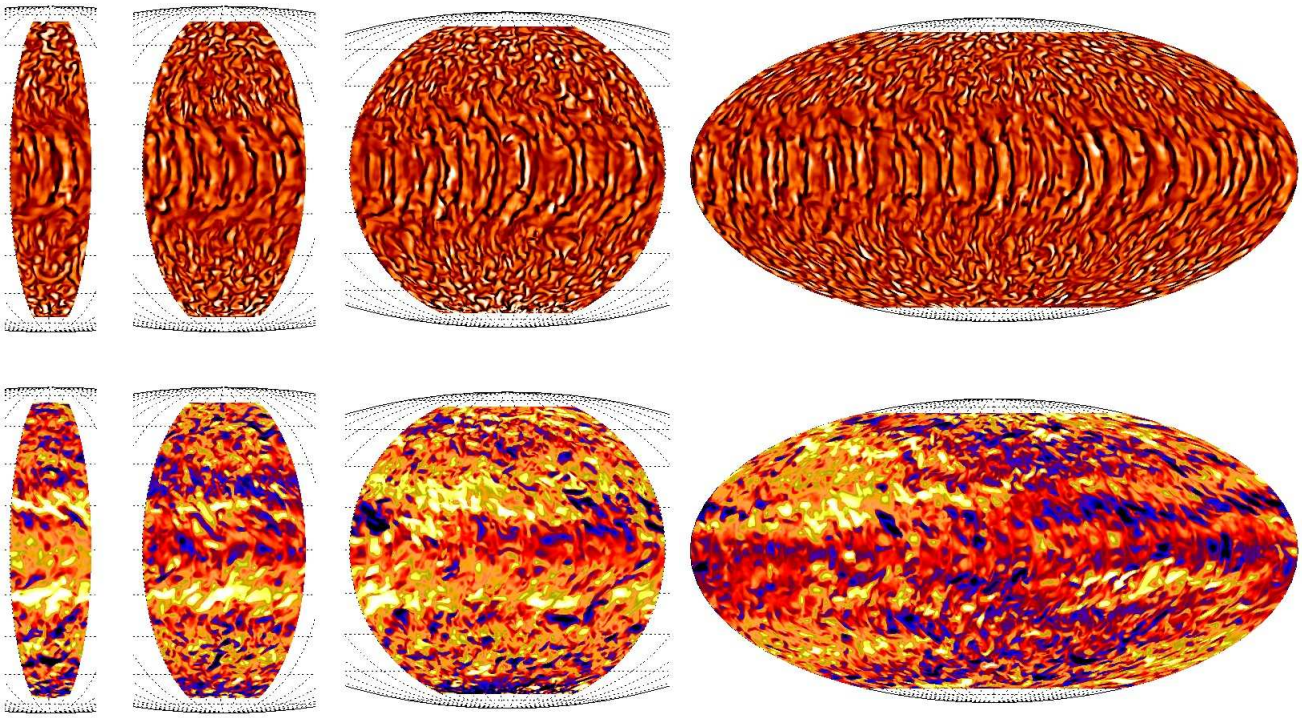

FIG. 12.— Radial velocity u_r (top row) and toroidal magnetic field (bottom) near the surface of the star $r = 0.98\,R$ in Mollweide projection from a Runs E1 (left), E2, E3, and E4 (right).

3.5. *Effect of domain size*

We recently reported equatorward migration of activity belts in a spherical wedge simulation (Käpylä et al. 2012a). There we gave results from simulations with a ϕ-extent of $\pi/2$. However, at large values of the Coriolis number, the α effect becomes sufficiently anisotropic and differential rotation weak so that nonaxisymmetric solutions become possible; see Moss & Brandenburg (1995) for corresponding mean-field models with dominant $m = 1$ modes in the limit of rapid rotation. To allow for such modes, we now choose a ϕ-extent of up to 2π. In the present case, we find that for $\mathrm{Co} \approx 7.8$ it is possible that non-axisymmetric dynamo modes of low azimuthal order ($m = 1$ or 2) can be excited. This would not be possible in the simulations of Käpylä et al. (2012a). The same applies to non-axisymmetric modes excited in hydrodynamic convection (e.g. Busse 2002; Brown et al. 2008; Käpylä et al. 2011b; Augustson et al. 2012).

We test the robustness of this result by performing runs with $\Delta\phi = \pi/4, \pi/2, \pi$, and 2π with otherwise identical parameters. We find that the same dynamo mode producing equatorward migration is ultimately excited in all of these runs. The only qualitatively different run is that with $\phi_0 = 2\pi$ where the poleward mode near the equator grows much faster than in the other cases. However, after $tu_{\rm rms}k_{\rm f} \approx 1500$ the equatorward mode takes over similarly as in the runs with a smaller ϕ_0.

The velocity field shows no marked evidence of non-axisymmetry but there are indications of $m = 1$ structures in the instantaneous magnetic field; see Figure 12. This is also reflected by the fraction of the axisymmetric component of the total magnetic energy, see the 5th and 6th columns of Table 2. We find that the energy of the mean toroidal field decreases monotonically when ϕ_0 is increased so that there is a factor of three difference between the extreme cases of Runs E1 and E4. The axisymmetric component still exhibits an oscillatory mode with equatorward migration in all runs in Set E.

We compute power spectra of the toroidal component of the magnetic field from the Run E4 over three 10° latitude strips from each hemisphere, centered around latitudes $\pm25^\circ$, $\pm45^\circ$ and $\pm65^\circ$. The results for the three lowest modes are shown in Figure 13. We find that at low ($\pm25^\circ$) and high ($\pm65^\circ$) latitudes the axisymmetric ($m = 0$) mode begins to dominate after around 1000 turnover times and shows a cyclic pattern consistent with that seen in the time-latitude diagram of the azimuthally averaged field. After $tu_{\rm rms}k_{\rm f} \approx 1600$, however, the $m = 1$ mode becomes stronger in the southern hemisphere. This coincides with the growth of the $m = 1$ mode at mid-latitudes where it dominates already earlier in both hemispheres. This is in rough agreement with some observational results of rapid rotators, which show the most prominent non-axisymmetric temperature (e.g. Hackman et al. 2001; Korhonen et al. 2007; Lindborg et al. 2011) and magnetic structures (Kochukhov et al. 2013) at the latitudinal range around 60–80°, while the equatorial and polar regions are more axisymmetric; some temperature inversions even show almost completely axisymmetric distributions in the polar regions and rings of azimuthal field at low latitudes (e.g. Donati et al. 2003). The strength of the axisymmetric versus the non-axisymmetric component has also been reported to vary over time with a time scale of a few years (Kochukhov et al. 2013).

3.6. *Irradiance variations*

The black body boundary condition allows the temperature vary at the surface of the star and thus enables the study of irradiance variations due to the magnetic cycle. In Figure 14 we show for Run C1 the difference between the azimuthally av-

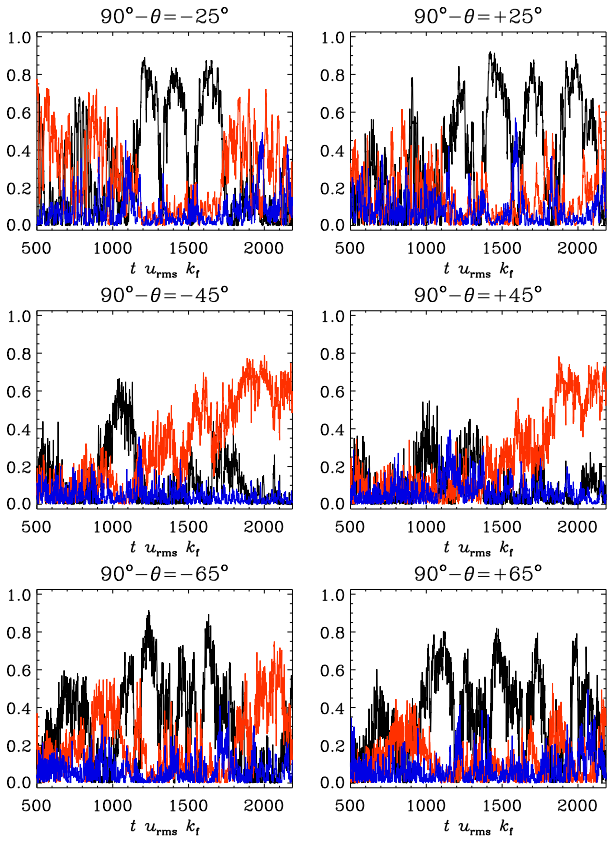

FIG. 13.— Energies of the $m = 0$ (black lines), 1 (red), and 2 (blue) modes of the toroidal magnetic field as functions of time near the surface of the star ($r = 0.98\,R$) in Run E4. The data is averaged over 10° latitude strips centered at latitudes $90^\circ - \theta = \pm 25$ (top panels), ± 45 (middle), and ± 65 (bottom) degrees and normalized by the total energy within each strip.

eraged temperature and its temporal average for the saturated state of the dynamo. We find a clear signal which is strongest for the poleward branch at high latitudes but also visible for the equatorward branch near the equator. The peak values at high latitudes are up to 20 per cent of the surface temperature. This is relatively large compared with earlier work using mean-field models (Brandenburg et al. 1992), which showed remarkably little relative variation of the order of 10^{-3} in the bulk of the convection zone and even less at the surface. This difference is probably related to the importance of latitudinal variations that were also present in the mean-field model of Brandenburg et al. (1992) and referred to as thermal shadows (Parker 1987).

4. CONCLUSIONS

We have studied the effects of density stratification on the dynamo solutions found in simulations of rotating turbulent convection in spherical wedge geometry. For the four values of Γ_ρ, which is the ratio of the densities at the bottom and at the surface of the convection zone. In addition, we vary the rotation rate for each value of Γ_ρ. For all stratifications we find quasi-steady large-scale dynamos for lower rotation and oscillatory solutions when rotation is rapid enough. The transition from quasi-steady to oscillatory modes seems to occur at a lower Co for higher stratification. Furthermore, for low values of Γ_ρ the oscillatory solutions show only poleward propagation of the activity belts whereas in higher Γ_ρ an equatorward branch appears at low latitudes.

The equatorward branch was first noticed by Käpylä et al.

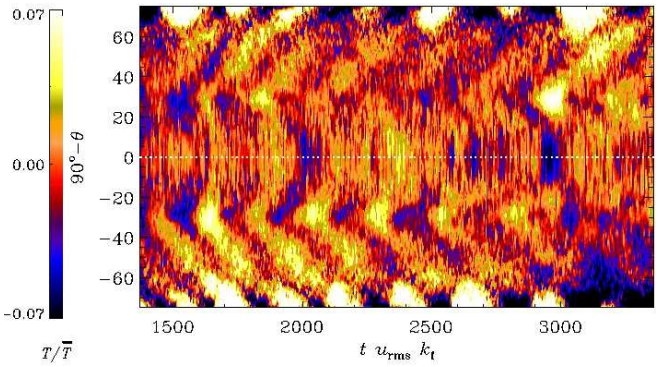

FIG. 14.— Temperature fluctuation at the surface from Run C1. The values are saturated at 7 per cent of the mean, whereas the maxima at high latitudes are around 20 per cent. The white dotted line denotes the equator.

(2012a) using a wedge with $\Delta\phi = 90^\circ$ longitude extent. Here we test the robustness of this result by varying $\Delta\phi$ from 45° to full 360°. We find a very similar pattern of the axisymmetric component of the field in all cases. However, the energy of the axisymmetric magnetic field decreases with increasing $\Delta\phi$. In the simulation with the full 2π ϕ-extent we observe an $m = 1$ mode which is visible even by visual inspection of the simulation data (see Figure 12). Such field configurations have been observed in rapidly rotating late-type stars (see e.g. Kochukhov et al. 2013) and our simulation is the first time such features have been seen in direct numerical simulations. We are currently investigating the rapid rotation regime with more targeted runs which will be reported in a separate publication (Cole et al. 2013, in preparation).

The ratio between cycle to rotation frequency, $\omega_{\rm cyc}/\Omega_0$, is argued to be an important non-dimensional output parameter of a cycle dynamo. For the Sun and other relatively inactive stars, this ratio is around 0.01, while for the more active stars it is around 0.002. For our models we find values in the range 0.002–0.01, but for most of the runs it is around 0.004. Although it is premature to make detailed comparisons with other stars and even the Sun, it is important to emphasize that kinematic mean-field dynamos produce the correct cycle frequency only for values of the turbulent magnetic diffusivity that are at least 10 times smaller than what is suggested by standard estimates (Choudhuri 1990). In our case, these longer cycle periods (or smaller cycle frequencies) are a result of nonlinearity and are only obtained in the saturated regime of the dynamo. The detailed reason for this is unclear, but it has been speculated that it is connected with a slow magnetic helicity evolution (Brandenburg 2005). Equally unclear is the reason for equatorward migration, which, as we have seen, is a consequence of nonlinearity, too. It will therefore be important to provide an accurate determination of all the relevant turbulent transport coefficients.

The simulations were performed using the supercomputers hosted by CSC – IT Center for Science Ltd. in Espoo, Finland, who are administered by the Finnish Ministry of Education. Financial support from the Academy of Finland grants No. 136189, 140970 (PJK) and 218159, 141017 (MJM), as well as the Swedish Research Council grant 621-2007-4064, and the European Research Council under the AstroDyn Research Project 227952 are acknowledged as well as the HPC-Europa2 project, funded by the European Commission - DG Research in the Seventh Framework Programme under grant agreement No. 228398. The authors thank NORDITA for hos-

pitality during their visits.

REFERENCES

Arlt, R., Sule, A., & Rüdiger, G. 2005, A&A, 441, 1171
Augustson, K. C., Brown, B. P., Brun, A. S., Miesch, M. S., & Toomre, J. 2012, ApJ, 756, 169
Brandenburg, A. 2005, ApJ, 625, 539
Brandenburg, A., Moss, D., & Tuominen, I. 1992, A&A, 265, 328
Brandenburg, A., Saar, S. H., & Turpin, C. R. 1998, ApJ, 498, L51
Brown, B. P., Browning, M. K., Brun, A. S., Miesch, M. S., & Toomre, J. 2008, ApJ, 689, 1354
—. 2010, ApJ, 711, 424
Brown, B. P., Miesch, M. S., Browning, M. K., Brun, A. S., & Toomre, J. 2011, ApJ, 731, 69
Brun, A. S., Miesch, M. S., & Toomre, J. 2004, ApJ, 614, 1073
Busse, F. H. 2002, Physics of Fluids, 14, 1301
Choudhuri, A. R. 1990, ApJ, 355, 733
Choudhuri, A. R., Chatterjee, P., & Jiang, J. 2007, Physical Review Letters, 98, 131103
Dikpati, M., & Charbonneau, P. 1999, ApJ, 518, 508
Dikpati, M., & Gilman, P. A. 2006, ApJ, 649, 498
Donati, J.-F., et al. 2003, MNRAS, 345, 1145
D'Silva, S., & Choudhuri, A. R. 1993, A&A, 272, 621
Ghizaru, M., Charbonneau, P., & Smolarkiewicz, P. K. 2010, ApJ, 715, L133
Gilman, P. A. 1983, ApJS, 53, 243
Glatzmaier, G. A. 1985, ApJ, 291, 300
Guerrero, G., & Käpylä, P. J. 2011, A&A, 533, A40
Hackman, T., Jetsu, L., & Tuominen, I. 2001, A&A, 374, 171
Hathaway, D. H. 2011, arXiv:1103.1561
Käpylä, P. J., Korpi, M. J., & Brandenburg, A. 2009, A&A, 500, 633
Käpylä, P. J., Korpi, M. J., Brandenburg, A., Mitra, D., & Tavakol, R. 2010, Astron. Nachr., 331, 73
Käpylä, P. J., Korpi, M. J., & Tuominen, I. 2004, A&A, 422, 793
—. 2006, Astron. Nachr., 327, 884
Käpylä, P. J., Mantere, M. J., & Brandenburg, A. 2011a, Astron. Nachr., 332, 883
—. 2012a, ApJ, 755, L22
—. 2012b, Geophys. Astrophys. Fluid Dyn., in press, arXiv:1111.6894
Käpylä, P. J., Mantere, M. J., Guerrero, G., Brandenburg, A., & Chatterjee, P. 2011b, A&A, 531, A162
Kitchatinov, L. L., & Olemskoy, S. V. 2012, Sol. Phys., 276, 3
Kitchatinov, L. L., Pipin, V. V., & Rüdiger, G. 1994, Astron. Nachr., 315, 157
Kitchatinov, L. L., & Rüdiger, G. 2005, Astron. Nachr., 326, 379
Kochukhov, O., Mantere, M. J., Hackman, T., & Ilyin, I. 2013, A&A, in press, arXiv:1301.1680
Korhonen, H., Berdyugina, S. V., Hackman, T., Ilyin, I. V., Strassmeier, K. G., & Tuominen, I. 2007, A&A, 476, 881
Krause, F., & Rädler, K.-H. 1980, Mean-field Magnetohydrodynamics and Dynamo Theory (Oxford: Pergamon Press)
Lindborg, M., Korpi, M. J., Hackman, T., Tuominen, I., Ilyin, I., & Piskunov, N. 2011, A&A, 526, A44
Malkus, W. V. R., & Proctor, M. R. E. 1975, Journal of Fluid Mechanics, 67, 417
Miesch, M. S., Brun, A. S., & Toomre, J. 2006, ApJ, 641, 618
Miesch, M. S., Elliott, J. R., Toomre, J., Clune, T. L., Glatzmaier, G. A., & Gilman, P. A. 2000, ApJ, 532, 593
Miesch, M. S., Featherstone, N. A., Rempel, M., & Trampedach, R. 2012, ApJ, 757, 128
Mitra, D., Tavakol, R., Brandenburg, A., & Moss, D. 2009, ApJ, 697, 923
Moss, D., & Brandenburg, A. 1995, Geophys. Astrophys. Fluid Dyn., 80, 229
Nelson, N. J., Brown, B. P., Brun, A. S., Miesch, M. S., & Toomre, J. 2013, ApJ, 762, 73
Ossendrijver, M. 2003, A&A Rev., 11, 287
Parker, E. N. 1955a, ApJ, 122, 293
—. 1955b, ApJ, 121, 491
—. 1987, ApJ, 321, 984
Pipin, V. V. 2012, IAU 294 proceedings, arXiv:1211.2426
Pipin, V. V., & Seehafer, N. 2009, A&A, 493, 819
Racine, É., Charbonneau, P., Ghizaru, M., Bouchat, A., & Smolarkiewicz, P. K. 2011, ApJ, 735, 46
Rempel, M. 2005, ApJ, 622, 1320
Robinson, F. J., & Chan, K. L. 2001, MNRAS, 321, 723
Saar, S. H., & Brandenburg, A. 1999, ApJ, 524, 295
Schou, J., et al. 1998, ApJ, 505, 390
Warnecke, J., Käpylä, P. J., Mantere, M. J., & Brandenburg, A. 2012, Sol. Phys., 280, 299
—. 2013, ApJ, submitted, arXiv:1301.2248